

SRNN: Spatiotemporal Relational Neural Network for Intuitive Physics Understanding

Fei Yang
 CogBeauty Lab
 yftadyz@163.com

Abstract

Human prowess in intuitive physics remains unmatched by machines. To bridge this gap, we argue for a fundamental shift towards brain-inspired computational principles. This paper introduces the Spatiotemporal Relational Neural Network (SRNN), a model that establishes a unified neural representation for object attributes, relations, and timeline, with computations governed by a Hebbian “Fire Together, Wire Together” mechanism across dedicated *What* and *How* pathways. This unified representation is directly used to generate structured linguistic descriptions of the visual scene, bridging perception and language within a shared neural substrate. Moreover, unlike the prevalent “pretrain-then-finetune” paradigm, SRNN adopts a “predefine-then-finetune” approach. On the CLEVRER benchmark, SRNN achieves competitive performance. Our analysis further reveals a benchmark bias, outlines a path for a more holistic evaluation, and demonstrates SRNN’s white-box utility for precise error diagnosis. Our work confirms the viability of translating biological intelligence into engineered systems for intuitive physics understanding.

1 Introduction

Human beings possess a remarkable ability to understand and interact with the physical world, underpinned by a core component of human intelligence known as intuitive physics [39; 25]. This innate capability allows us to form rich mental representations of objects and their spatiotemporal relationships. Even in infancy, humans demonstrate a sophisticated grasp of intuitive physics: they can discern object boundaries from visual input, mentally reconstruct the complete shapes of objects that become partially or fully occluded, and accurately anticipate the trajectories and final resting places of moving objects [42].

The computer vision community has made significant progress in enabling machines to acquire

this capability [1; 45; 52; 20; 11]. However, their performance on visual cognitive understanding tasks still pales in comparison to human-level competence [30; 32]. To bridge this gap, we propose that a fundamental shift is necessary: we must look to the brain—the only proven general visual cognitive system—as an unparalleled blueprint. Our research, therefore, aims to identify the brain’s core computational principles and implement them in artificial neural networks, thereby translating this biological success into engineered general intelligence.

Our model, the Spatiotemporal Relational Neural Network (SRNN), establishes a unified spatiotemporal representation in which object attributes (shape/texture/color), relations (touch, distance change, direction change, and kinematic states), and time are directly encoded as neurons. The core computation of forming this representation follows the Hebbian principle, often summarized as *Fire Together, Wire Together* [17]. This mechanism, mediated by stamp neurons, operates concurrently across three key components: a *How* pathway for object relations, a *What* pathway for object attributes, and a temporal binding process for timeline construction. Furthermore, SRNN extends this unified representation to bridge perception with language. Prevailing methods in AI often connect video and language by projecting both into a shared embedding space [33]. In contrast, the human brain seamlessly links visual perception and language through a network of interconnected neurons. Inspired by this architecture, SRNN directly grounds language generation in the same neural substrate that represents spatiotemporal concepts.

In contrast to the prevalent “pretrain-then-finetune” paradigm [4; 51; 44]—where a base model is first pre-trained on massive-scale data and subsequently fine-tuned with limited high-quality samples for downstream tasks—our SRNN adopts a “predefine-then-finetune” approach: it architec-

turally hard-codes human cognitive priors at the outset. This foundational design allows the model’s parameters to be efficiently tuned from only a handful of samples.

We evaluate SRNN on the CLEVRER [49] benchmark, a dataset comprising 20,000 synthetic videos of object collisions designed to probe physical reasoning. In our experiments, SRNN first generates a structured textual description for each video. This description, along with a question, is then processed by a large language model (LLM) to derive the final answer. Experimental results demonstrate that SRNN achieves competitive accuracy on CLEVRER, confirming its ability to effectively capture and encode essential spatiotemporal relations from visual stream. Moreover, a cognitive ablation study reveals a significant bias in the CLEVRER benchmark: its question distribution does not comprehensively cover the fundamental elements of human physical cognition. To address this gap, we outline a pathway—illustrated with concrete examples—toward constructing a more holistic benchmark for evaluating machines on human-like physical cognition. Finally, the white-box nature of SRNN enables us to precisely pinpoint the root cause of errors in every sampled case, revealing a diverse set of failure modes—from relational misidentification to LLM errors—that are often obscured in end-to-end black-box models. Code and models will be made publicly available soon.

2 Relative Work

Intuitive Physics. This topic refers to the implicit, informal expectations and understandings about the functioning of the physical world that humans possess prior to formal education [38; 2; 7]. Cognitive science provides experimental evidence that humans, even in infancy, can comprehend touch [29], distance change [36], direction change [37], and kinematic states [23]. For example, infants show surprise when an object spontaneously begins moving from rest, as this violates the expectation that external force is required to initiate movement from a stationary state [3]. Machines must first comprehend these basic relationships that serve as the cornerstones of human cognition.

Visual Processing. Neurological evidence suggests that the human visual system decomposes the incoming spatiotemporal stream of information into two distinct pathways [16; 24]. The ven-

tral stream (What Pathway) processes static object properties like color and shape, which are selectively attended to and bound to a coherent object representation through attentional mechanisms [40]. The dorsal stream (How Pathway) processes spatial location and motion. This information is processed in a hierarchical manner, from low-level features to complex representations [14]. Crucially, the brain shapes its complex representations via a process where frequently co-activated neurons strengthen their connections—a process often summarized as “neurons that fire together, wire together” [17]. When describing the visual scene, these integrated signals are routed to language networks for interpretation, where conceptual semantics are processed in Wernicke’s area and structured sentences are generated via Broca’s area [18]. The architecture of our SRNN embodies the above neurological principles of human dynamic scene understanding, representing a functional, computational neuro-mimetic approach.

Intuitive Physics Reasoning Task. Neurosymbolic approaches have been widely explored for this task. NS-DR [50] represents the spatiotemporal relations of each frame in a video as a directed graph. However, a unified spatiotemporal graph is absent, as NS-DR does not have nodes to represent time or static attributes of an object. Moreover, unlike human brain, where relational concepts are stored in neuronal assemblies [35], NS-DR uses edges to represent these concepts. DCL [10] and VRDP [10] represent the spatiotemporal relations in each frame of a video as a couple of matrix where each element stands for a numerical confidence score. Object attribute (e.g. shape, color) and relational concepts (e.g. collision) are represented as embedding vectors, thereby being able to optimize a goal function through backpropagation. In terms of representation and computation, the above methods are much different from human brain.

For end-to-end approaches, Object-based Attention [12] designs a transformer-based neural network for spatio-temporal reasoning about videos. All components are updated by self-supervised learning. In [28], convolutional neural networks are trained to understand the physical intuition presented in block tower videos. Although the architecture of these neural networks have similarities with human brain, the computational mechanisms underlying neuron connection weights are funda-

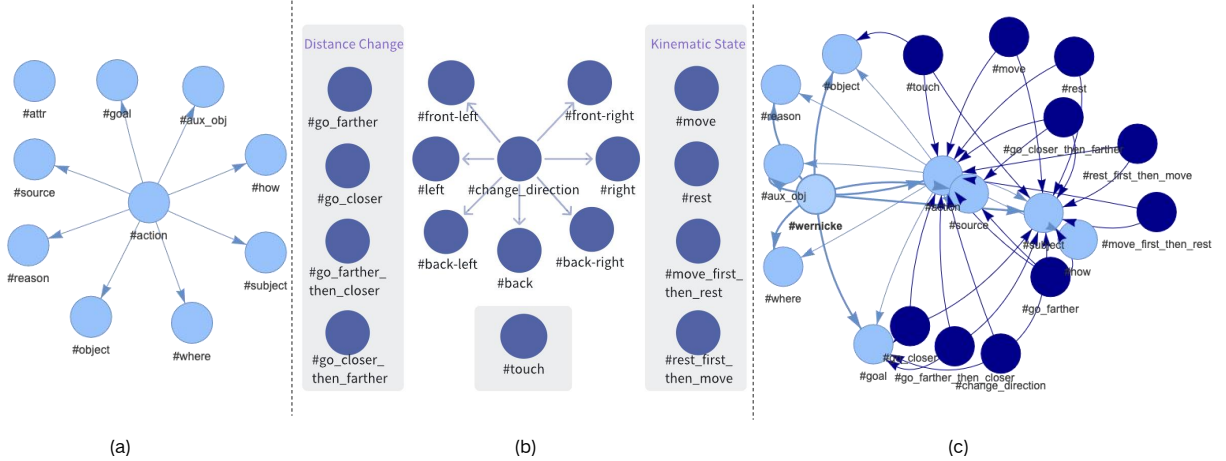


Figure 1: (a) Semantic Nature Design. The core of this design is `#action` which connects eight semantic roles. (b) Spatial Nature Design. For `#change_direction`, we add `#relation_attr` neurons (e.g. `#right`, `#left`, `#back`, etc.) to indicate its attributes. For other relations, `#relation_attr` does not exist. (c) Connections between spatial neurons and semantic neurons. The neuron `#wernicke` makes the semantic neurons capable of being activated when language is necessary. All neurons are depicted in blue to indicate their inactive state.

mentally distinct from the Hebbian principle.

Among existing benchmarks for intuitive physical reasoning [49; 9; 15; 34; 6; 5; 41], we evaluate SRNN on CLEVRER [49]. This dataset contains 15,000 five-second videos showing object interactions, with objects defined by three static attributes—shape, texture, and color—and undergoing linear motion without magnetic forces. CLEVRER includes four types of questions: (1) predictive, requiring forecasting of future relations; (2) counterfactual, exploring alternative scenarios by removing objects; (3) descriptive, involving identification of current attributes and relationships; and (4) explanatory, demanding cause identification for observed relations. The collision events in CLEVRER are interpreted as touch relations in this work. We exclude other benchmarks due to elements uncommon in daily human scenes or visual complexity beyond our research scope. For instance, ComPhy [9] introduces charge-based attraction and repulsion, while CATER [15] involves object levitation.

3 SRNN

SRNN first boots spatial and semantic nature designs to predefine its neural network architecture. After that, it begins to watch a video. For each frame of the video, it perceives static states of objects. The attributes of shape, texture and color are attended. In the meanwhile, pixel coordinates of object centers are transformed into 3D camera coordinates by depth estimation. We track these camera

coordinates to form object trajectories. Then it perceives spatiotemporal relations between each pair of objects given their trajectories within a time slot. After that, neurons are fired and wired, which occurs simultaneously within three key components: the `how` pathway for object relations, the `what` pathway for object attributes, and the temporal binding for timeline construction. A semantic network is also activated and generates sentences to describe the video.

3.1 Loading Nature Design

SRNN initializes its cognitive architecture by loading a predefined neural network called Nature Design. We adopt a core distinction between the propensity that humans inherit since they are born (Nature Design) and knowledge acquired from developmental experiences (Nurture Belief) [47]. The Nature Design mainly includes two parts: spatial neurons and semantic neurons, which are presented in Fig. 1 (a) and (b), respectively. The semantic part draws inspiration from PropNet architecture as described in [48]. Fig. 1 (c) shows the connections between spatial neurons and semantic neurons. Before watching a video, all these neurons are in an inactive state.

3.2 Perceiving Static States

We mimic human attention mechanism to attend to and integrate multiple visual attributes into coherent object percepts. First when SRNN receives the frame data of a video, it obtains detection results

for shape and texture of objects using YOLO-based models. Then cross-modal binding is performed by calculating the Intersection-over-Union (IoU) between shape and texture bounding boxes. Only detection pairs exceeding an IoU threshold are considered. Each region’s dominant color is extracted by aggregating RGB values. When shape and texture boxes overlap significantly and share the same color perception, their features are merged into a unified object representation with a composite label (e.g., “blue_metal_sphere”).

To support estimating the distance between objects in 3D space, we convert frame image pixels into egocentric camera coordinates. For each pixel at position (u, v) , the depth value is computed by an opensource tool named Video Depth Anything [8]. The focal length of the camera is estimated by GeoCalib [43]. The process of computing camera coordinates (x, y, z) is described by:

$$\begin{aligned} x &= \frac{(u - c_x) \cdot z}{f} \\ y &= \frac{(v - c_y) \cdot z}{f} \\ z &= d(u, v) \end{aligned} \quad (1)$$

where $z = d(u, v)$ is the depth (distance from the camera plane) at pixel (u, v) and f is the focal length (in pixels) of the camera. The c_x, c_y are the coordinates of the principal point (the optical center of the image). We perform 3D scene reconstruction by back-projecting all pixels into a point cloud using MeshLab. The metric consistency and geometric plausibility of the derived egocentric coordinates are confirmed. Finally, the Euclidean distance between object centers is computed for each pair of objects appearing in the frame given their camera coordinates.

3.3 Perceiving Spatiotemporal Relations

Object tracking is performed based on bounding box overlap and class consistency across consecutive frames. Detections that fail to match any stored trace initiate a new object entity.

We split the video into non-overlapping time slots. Each time slot contains an equal number of consecutive frames. Within each slot, object relations are computed from the object trajectories and the distance arrays between objects. In this work, we focus on four relations: the kinematic profile of an object, direction change of an object, distance change between two objects, and touch

between two objects.

Kinematic Profile of an Object. The kinematic state of an object—whether it is moving or at rest—is determined by analyzing its trajectory over a sequence of frames. Specifically, we calculate the Euclidean distance between the center positions in the first and the last frame. If this net displacement exceeds a threshold parameter, the object is classified as `#move`; otherwise it is classified as `#rest`. For more granularity, the trajectory of `#move` object is split into two equal-length segments to detect transitional states `#rest_first_then_move` or `#move_first_then_rest`.

Direction Change of an Object. Direction change is determined by comparing the principal movement vectors of an object’s trajectory before and after a touch. The signed angle between these vectors is computed, and a direction change occurs if the magnitude of the angle surpasses a threshold. Seven directions are predefined: `front-right`, `right`, `back-right`, `back`, `back-left`, `left`, `front-left`. The angular variation range for each direction is provided in App. C.

Distance Change Between Two Objects. A distance change occurs once the variation amplitude of the distance array exceeds a predefined threshold. Then we identify trend patterns by analyzing variations in differences between adjacent elements in the distance array. Four trends are defined: `#go_closer`, `#go_farther`, `#go_farther_then_closer`, and `#go_closer_then_farther`. If the minimum distance between the two objects exceeds a given threshold, the trend is not attended. As the time slot is very short and object jittering does not exist, no other distance trends remain.

Touch Between Two Objects. When the inter-object distance falls below a touch threshold, auxiliary motions are further examined to confirm touch. At least one object in the pair under inspection must either exhibit a change in moving direction or transition from a stationary to moving state. To enhance reliability, we also enforce an isolation condition: neither object should be close to a third object below the touch threshold within the time slot, reducing false positives in crowded scenes. Since the time slot is extremely short, this condition does not noticeably reduce the recall of touches.

The threshold parameters for each relation are determined in a human-driven fashion to ensure alignment with human perception. Specifically, we

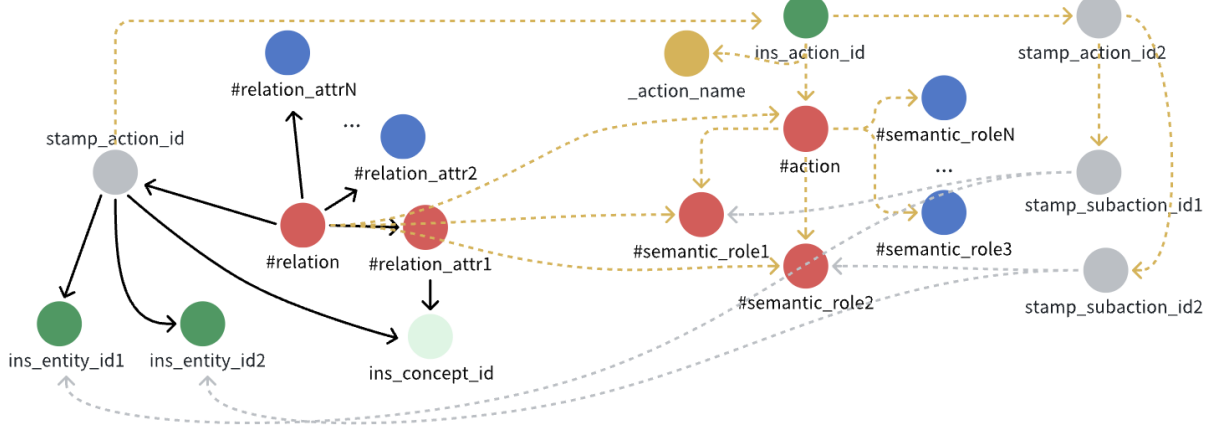


Figure 2: The Fire-and-Wire Mechanism (left) and the Language Generation Module (right) in the How Pathway. **Left:** Visual perceptions activate a relational neuron $\#relation$ along with creation and activation of entity-instance neurons ins_entity_id1 and ins_entity_id2 . Then $\#relation$ triggers the creation and activation of an action-stamp neuron $stamp_action_id$ which binds ins_entity_id1 and ins_entity_id2 . If relational attributes exists for this relation, the corresponding $\#relation_attr1$ is activated by $\#relation$. A concept-instance neuron $ins_concept_id1$ is pointed by $\#relation_attr1$ and $stamp_action_id$. Other neurons below the activation threshold remain inactive (shown in blue). **Right:** The $stamp_action_id$ neuron triggers ins_action_id , which acts as the starting point of the semantic network. Connections are formed between ins_action_id and its lexical neuron $_action_name$, as well as with $\#action$. Meanwhile, $\#relation$ propagates signals to $\#action$ and $\#semantic_roles$ via predefined neural pathways in Nature Design. Joint signals from ins_action_id and $\#relation$ activates $\#action$, which in turn send signals to all the semantic-role neurons. Only $\#semantic_role1$ and $\#semantic_role2$ are activated upon receiving sufficient signals. Finally, $stamp_subaction_id1$ wires $\#semantic_role1$ and ins_entity_id1 , and $stamp_subaction_id2$ binds $\#semantic_role2$ and ins_entity_id2 .

calibrate these parameters on a handful of videos and then validate the computational results against human judgments. The tuning process is illustrated in App. B.

3.4 Firing and Wiring Neurons

Inspired by the neurobiological concept that “synchronous firing strengthens synaptic connections” [17], we designed a representation mechanism where SRNN processes visual inputs by activating relevant neurons (*Fire*) and then establishing connections between these activated neurons (*Wire*). This process encodes both how entities interact or change over time and what attributes of entities are present in the neural network.

Each neuron possesses a threshold and becomes activated when its cumulative input within a time slot reaches this threshold, subsequently emitting a signal. Signals propagate along directed connections to other neurons. All neurons emit signals with a value of 1.

How Pathway.

Neurons (e.g., $\#move$, $\#touch$) are activated by the observed corresponding relations. All participant instances involved in these relations are rep-

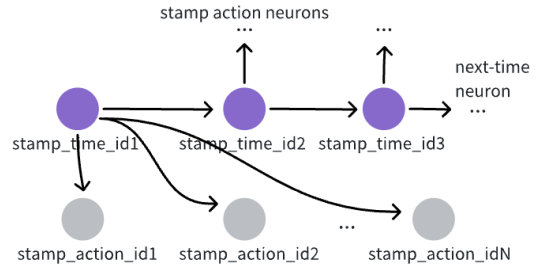


Figure 3: The Fire-and-Wire Mechanism in the Temporal Binding. The temporal neuron $stamp_time_id1$ marks the origin of the timeline and points to $stamp_time_id2$. All action-stamp neurons present during this temporal window are associated with $stamp_time_id1$. As time progresses, new temporal neurons are generated, activated, and linked sequentially to form an ordered chain.

resented by entity-instance neurons which simultaneously receive activation. When a relation neuron fires, it triggers the creation of an action-stamp neuron, which connects all the participating entities of the relation. The left network of Fig. 2 details this process.

Temporal Binding. A unique time-stamp neuron is generated for each time slot, sequentially

linked to the previous time-stamp neuron. This neuron connects all action-stamp neurons within the same time slot, binding co-occurring relations into a coherent episodic memory trace. The details of this process are depicted in Fig. 3.

What Pathway. For each entity detected in the relations, its attended attributes like color and texture are represented by concept-instance neurons which are linked by `#attr`. When the entity neuron fires, it triggers the creation of an entity-stamp neuron, which connects all the attribute neurons of the entity. Fig. 4 illustrates the process details.

3.5 Generating Language Description

The language module generates a sentence description for each relation. It contains two components: a semantic network and a sentence generator. The semantic network fulfills three primary functions: (1) assigning lexical labels to objects; (2) assigning verbal labels to relations; and (3) assigning semantic roles like agent and patient to the participants involved in a relation. In this project, the moving object in a relation serves as the agent. We present this semantic network in detail in Fig. 2 and Fig. 4 with yellow dashed lines. The implementation of the semantic network draws inspiration from the approach outlined in [48].

A key distinction lies in our introduction of subaction-stamp neurons to bind semantic roles and instance entities, thereby explicitly defining the relationship between entities and their corresponding roles.

The sentence generator takes the semantic network as input and generates a sentence. A sentence structure is sequentially constructed by positioning the agent entity first, followed by the relation lemma, patient entity (if present), and goal or source entities introduced by the prepositions “to” or “from” respectively. Entity attributes are incorporated by querying associated concept neurons to enrich descriptions with conceptual features (e.g., color, texture). The final sentence is generated by concatenating all components into a fluent string. For example, “the rubber gray sphere `ins_entity_39` touch rubber yellow sphere `ins_entity_37`”

3.6 Predicting Future Relations

To make SRNN be able to handle counterfactual and predictive questions from CLEVRER, we add this module to predict if an object will touch another object in the next time slot or after the video ends. This algorithm employs PCA [22] to identify

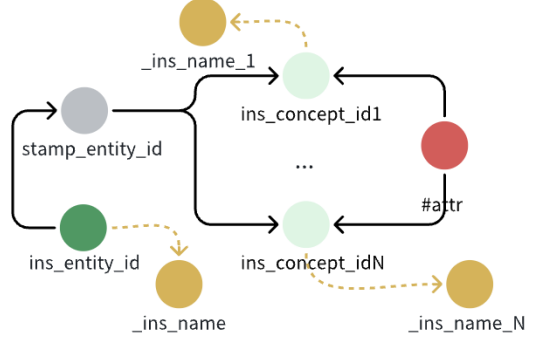


Figure 4: The Fire-and-Wire Mechanism and the Language Generation Module in the What Pathway. The neuron `ins_entity_id` initiates the creation and activation of `stamp_entity_id`. Simultaneously, concept-instance neurons are created and activated to encode the entity’s attributes, which are then bound together by `stamp_entity_id`. These instance neurons, in turn, activate corresponding lexical neurons (indicated by yellow dashed lines), denoted as `_ins_name`.

the principal direction of motion from 3D trajectory data. It projects the trajectory onto this axis and applies linear regression to derive a constant-velocity model, assuming zero acceleration for straight-line motion prediction. Predictions are discarded for entity pairs initially beyond a distance threshold to ensure physically plausible forecasts. Predicted results are appended in text form following the output of Section 3.5.

In App. D, we provide an example that details the output of the aforementioned modules.

4 Experiments

We first demonstrate SRNN achieves competitive accuracy on the CLEVRER dataset, proving its effectiveness in capturing essential video information. Next, a cognitive ablation study is conducted to quantify the causal role of specific relations in video reasoning. This study also serves to audit inherent biases in CLEVRER for the development of a more comprehensive benchmark. Finally, a fine-grained error analysis is performed on incorrectly answered cases, leveraging the intrinsic interpretability of our model to categorize failure patterns and identify limitations.

4.1 Performance Comparison

We compare the performance of SRNN on CLEVRER against a comprehensive set of baselines, including: TVQA+ [27], Memory [13], IEP (V) [21], TbD-net (V) [31], HCRN [26], MAC (V+) [19], NS-DR [50], DCL [10], Object-based

Methods	Predictive		Counterfactual		Descriptive	Explanatory	
	per opt.	per ques.	per opt.	per ques.		per opt.	per ques.
TVQA+ [27]	70.3	48.9	53.9	4.1	72.0	63.3	23.7
Memory [13]	50.0	33.1	54.2	7.0	54.7	53.7	13.9
IEP (V) [21]	50.0	9.7	53.4	3.8	52.8	52.6	14.5
TbD-net (V) [31]	50.3	6.5	56.1	4.4	79.5	61.6	3.8
HCRN [26]	54.1	21.0	57.1	11.5	55.7	63.3	21.0
MAC (V+) [19]	59.7	42.9	63.5	25.1	86.4	70.5	22.3
NS-DR [50]	82.9	68.7	74.1	42.2	88.1	87.6	79.6
DCL [10]	90.5	82.0	80.4	46.5	90.7	89.6	82.8
Object-based Attention [12]	93.5	87.5	91.4	75.6	94.0	98.5	96.0
VRDP [10]	95.7	91.4	94.8	84.3	93.4	96.3	91.9
SRNN	81.0	62.9	84.7	58.0	89.2	90.5	80.0

Table 1: Comparison of question-answering accuracy on CLEVRER. The highest accuracy for each question type is highlighted in boldface. Scores are obtained from the original publications of each model. SRNN demonstrates notably competitive accuracy.

Attention [12], and VRDP [10]. Among these, VRDP [10] represents the state-of-the-art neuro-symbolic model, while Object-based Attention [12] is the state-of-the-art end-to-end approach.

Evaluation Metrics. We employ question answering accuracy as the evaluation metric. It is important to note that for the multi-choice questions (including explanatory, predictive, and counterfactual types), a question is considered correctly answered (per ques.) only if all its associated options (per opt.) are answered correctly.

Implementation Details. Each video is temporally segmented into five time slots, with each slot corresponding to a one-second duration. The video descriptions generated by our SRNN model are utilized as input for a Large Language Model (LLM) to answer the questions. Specifically, for a given video and a question, the textual descriptions from SRNN are concatenated into a prompt along with the question text. To ensure consistent comprehension between humans and the LLM, critical alignments of the question contexts are incorporated into the prompt. Furthermore, specific solving instructions are added to guide the LLM in reasoning through the problem based on the provided logic. All parameters and prompt alignments are tuned on ten videos from the CLEVRER training split, and the final performance is evaluated on the CLEVRER validation split. The results of key parameters are presented in App. B. YOLO training details are appended in App. A. LLM choice and its prompts are explained in App. E.

Results. As shown in Tab. 1, SRNN delivers a strong performance of 90.5% per option and 80.0%

per question for explanatory questions. This result places it as the third-best performing model in our comparison, after Object-based Attention (98.5% per opt., 96.0% per ques.) and VRDP (96.3% per opt., 91.9% per ques.). On descriptive questions, SRNN achieves 89.2% accuracy, a result that is on par with the top-performing models, slightly behind VRDP (93.4%). For Counterfactual questions, our method attains 84.7% per option and 58.0% per question, approaching Object-based Attention (91.4% per opt., 75.6% per ques.). These results collectively affirm SRNN’s effectiveness in capturing and encoding the essential relational information presented in a video, which is necessary for complex spatio-temporal and causal reasoning.

4.2 Cognitive Ablation

In this section, we perform a cognitive ablation study. Unlike conventional ablation that removes structural components of a model (e.g., layers or neurons), we remove the human-understandable physical concepts (e.g., touch, distance change) presented in the videos, to directly interrogate the causal role of specific relations in video reasoning. Moreover, we audit the biases of the CLEVRER dataset to provide a roadmap for designing a more comprehensive benchmark.

By selectively removing relational neurons in the neural network, such as `#touch`, corresponding physical concepts can be effectively stripped from the video. The resulting textual descriptions are then fed into LLM to answer questions and evaluate accuracy. The configurations of SRNN and LLM remain identical to those used in Sec. 4.1.

Ablation Dimension	Predictive		Counterfactual		Descriptive	Explanatory	
	per opt.	per ques.	per opt.	per ques.		per opt.	per ques.
-	81.0	62.9	84.7	58.0	89.2	90.5	80.0
Rest State	-1.8	-2.9	-0.1	-0.5	-4.8	-0.7	-0.2
Direction Change	-1.1	-2.2	-0.6	-2.7	-0.2	-0.4	-0.1
Distance Change	-0.3	-1.3	-0.3	-1.5	0.1	-0.3	-1.3
Touch	-2.9	-4.2	-15.9	-35.3	-15.2	-25.2	-40.8
Future Touch	-9.5	-16.7	-4.7	-12.6	0.2	-0.6	-0.5
Time Order	-25.3	-46.1	-7.1	-16.0	-18.9	-27.9	-49.1

Table 2: The first row presents the baseline accuracy, while the following rows display the decrease in accuracy upon the removal of each dimension. *Rest State* implies complete disregard for stationary objects.

Tab. 2 presents the changes in answer accuracy of the model when different types of relations are removed for various question categories.

Predictive Questions. The drastic performance drop from Time Order ablation (-25.3%/-46.1%) demonstrates that forecasting is critically dependent on a precise understanding of relation sequences. Furthermore, the significant impact of Future Touch ablation (-9.5%/-16.7%) confirms that the accuracy is directly driven by the capacity to anticipate imminent collisions. These results reveal that the predictive questions entirely fail to address stationary objects, alterations in object orientation, and variations in inter-object distances presented in the video.

Counterfactual Questions. The profound performance degradation resulting from Touch ablation (-15.9%/-35.3%) confirms that tangible collisions serve as the primary anchor for mental simulation. Concurrently, the notable impact of Time Order ablation (-7.1%/-16.0%) underscores that constructing coherent counterfactuals also requires altering the sequence of relations. These findings expose a pronounced bias in the CLEVRER dataset, where the counterfactual questions heavily rely on inverting or modifying contact-based interactions. To address this bias, the set of answer choices could be expanded to incorporate options based on other factors, such as kinematic state (e.g., “The yellow rubber object stays at rest after the blue cylinder is removed”) or changes in relative distance (e.g., “The yellow rubber object goes close to the red cube sphere after the blue cylinder is removed”).

Descriptive Questions. The severe performance degradation caused by Touch ablation (-15.2%) establishes that this type of questions places a significant emphasis on the touch interactions in the video. Concurrently, the substantial drop from Time Order

ablation (-18.9%) confirms that accurately describing object attributes and relations often necessitates an implicit understanding of the temporal context in which they occur. CLEVRER largely overlooks the roles of Direction Change and Distance Change. Future benchmarks should be extended to probe these under-represented concepts, such as “How many objects are moving away from the red metal sphere when the rubber object exits the scene” (Distance Change) or “Which direction does the yellow rubber object shift to after it touches the green cube” (Direction Change).

Descriptive questions also target static objects, such as “How many metal objects are stationary when the blue rubber object exits the scene” or “What color is the stationary rubber object”. The significant accuracy drop (-4.8%) directly confirms their important role in this task. In contrast, other types of questions show almost no performance drop after removing this factor, indicating that they do not rely on these static objects that serve as background. This also reveals a pronounced bias in the CLEVRER dataset.

Explanatory Questions. The severe accuracy drop from Time Order ablation (-27.9%/-49.1%) proves that causal attribution depends almost entirely on timing. This aligns with expectations, as explaining an event necessarily relies on its past temporal sequence. The major decline under Touch ablation (-25.2%/-40.8%) confirms that explanation prioritizes the touch relations in the video. This exposes a strong bias in CLEVRER, where the explanatory questions overwhelmingly focus on collision. A more balanced benchmark should incorporate questions involving non-contact influences, such as “Which of the following is responsible for the brown object’s going close to the purple object” (Distance Change) or “Which of

Table 3: Error type distribution (in %) across predictive (P), counterfactual (CF), descriptive (D), and explanatory (E) questions. The top three errors for each question type are highlighted in boldface.

Error Type	P	CF	D	E
Ambiguous Ground Truth	20	15	15	0
Annotation Error	0	5	10	5
Relation Timing Error	0	0	10	10
False Positive Touch	0	5	10	15
Friction Neglect	10	0	0	0
LLM Misunderstanding	5	5	10	5
LLM Incomplete Prompt	0	0	0	15
LLM Prompt Deviation	10	0	0	10
Missed Touch	10	55	10	35
Object Detection Failure	15	0	20	5
Occluded Collision Path	10	0	0	0
Out Of Attention	20	15	0	0
Question Misalignment	0	0	15	0

the following is responsible for the brown object’s changing direction to its left?" (Direction Change).

4.3 Error Analysis

We conduct a fine-grained error analysis to identify the limitations of SRNN on the CLEVRER dataset and to guide future improvements. For each question type, we randomly sample 20 incorrectly answered cases from Sec. 4.1, ensuring that each multi-choice problem appears only once. We then categorize the failure patterns and analyze their distribution across different question types.

A key advantage of our approach lies in its case-level interpretability. Unlike embedding methods that rely on opaque numerical representations, our model allows us to inspect individual neurons at each time slot via an interactive visualization interface. This capability enables us to precisely pinpoint the root cause of errors in every sampled case, revealing a diverse set of error types that would be difficult to discern in embedding models. Error types are defined as follows:

- **Ambiguous Ground Truth.** Human verifiers cannot reliably determine the correctness of the ground-truth answers in the benchmark.
- **Annotation Error.** The ground-truth answers for questions in the benchmark are incorrect.
- **Relation Timing Error.** Incorrect identification of the timing of relations, like misidentification of the sequence of two touches.
- **False Positive Touch.** SRNN anticipates a

touch relation that fails to occur in the video or after the video.

- **Friction Neglect.** Neglect of friction effects, leading to errors in the module of future touch prediction. This module assumes uniform linear motion only.
- **LLM Description Misunderstanding.** LLM misunderstands the video description text.
- **LLM Incomplete Prompt.** Incomplete reasoning logic in the prompt, preventing the LLM from outputting correct answers.
- **LLM Prompt Deviation.** LLM does not strictly follow the prompt’s guidance during problem-solving.
- **Missed Touch.** Failure to detect touch relations. It occurs when a collision is extremely minor, or when the object’s trajectory remains unaltered after a collision.
- **Object Detection Failure.** Failure to detect objects in some frames. This error primarily occurs when the YOLO models fail to detect objects or produce inaccurate detections.
- **Occluded Collision Path.** The path to collision is blocked by a third object, and this factor is not considered by our algorithm.
- **Out Of Attention.** Objects are too distant, so the future prediction module is not activated.
- **Question Misalignment.** A discrepancy exists between the intended meaning of the question and the LLM’s interpretation of it, leading to reasoning based on a misunderstood premise.

Based on the error distribution summarized in Tab. 3, we analyze the primary error types to identify the key bottlenecks of SRNN across different question categories.

Predictive Questions. The analysis reveals that the future prediction module is a primary bottleneck, accounting for approximately 50% of all errors. This is directly evidenced by the failure modes: Out Of Attention (20%), Occluded Collision Path (10%), Missed Touch (10%), and Friction Neglect (10%), which provides concrete directions for optimizing the future prediction component.

Counterfactual Questions. The primary bottleneck is Missed Touch (55%), where it fails to detect critical touch mentioned in questions. This error deprives the LLM of necessary contextual information, preventing correct answer generation.

Descriptive Questions. The main sources of error include Object Detection Failure (20%), Question Misalignment (15%), and Ambiguous Ground

Truth (15%). As this question type fundamentally relies on accurately describing scene content, failures in object recognition have an immediate and pronounced impact. Additionally, the diverse phrasing of descriptive questions introduces greater challenges in achieving semantic alignment between the LLM’s interpretation and the question’s intent.

Explanatory Questions. The primary challenge involves touch relation recognition, with Missed Touch (35%) and False Positive Touch (15%) constituting half of all errors. Both missing critical contacts and hallucinating non-existent ones corrupt the causal chain, depriving the LLM of the correct physical context required for generating valid explanations.

5 Conclusion

In this work, we propose the Spatiotemporal Relational Neural Network (SRNN), which unifies object attributes, relations, and timeline through a Hebbian learning mechanism across dedicated pathways. Experimental results on CLEVRER demonstrate that principles of biological intelligence can be successfully engineered to understand intuitive physics. Through cognitive ablation, we outline a path toward a more holistic evaluation by identifying and mitigating benchmark bias. Evolving its core set of relations into a richer repertoire following the human developmental path will enable SRNN to interpret human activities in daily life.

References

- [1] Shuai Bai, Keqin Chen, Xuejing Liu, Jialin Wang, Wenbin Ge, Sibo Song, Kai Dang, Peng Wang, Shijie Wang, Jun Tang, Humen Zhong, Yuanzhi Zhu, Mingkun Yang, Zhaohai Li, Jianqiang Wan, Pengfei Wang, Wei Ding, Zheren Fu, Yiheng Xu, Jiabo Ye, Xi Zhang, Tianbao Xie, Zesen Cheng, Hang Zhang, Zhibo Yang, Haiyang Xu, and Junyang Lin. Qwen2.5-vl technical report. *arXiv preprint arXiv:2502.13923*, 2025.
- [2] Renee Baillargeon. The development of infants’ intuition about support. *Early Development and Parenting*, 4(1):1–4, 2007.
- [3] Renée Baillargeon, Elizabeth S Spelke, and Stanley Wasserman. Object permanence in 3.5-and 4.5-month-old infants. *Developmental psychology*, 23(5):655–664, 1987.
- [4] Federico Baldassarre, Marc Szafraniec, Basile Terver, Vasil Khalidov, Francisco Massa, Yann LeCun, Patrick Labatut, Maximilian Seitzer, and Piotr Bojanowski. Back to the features: Dino as a foundation for video world models. *arXiv preprint arXiv:2507.19468*, 2025.
- [5] D. M. Bear, E. Wang, D. Mrowca, F. J. Binder, H.-Y. F. Tung, R. Pramod, C. Holdaway, S. Tao, K. Smith, and F.-Y. Sun et al. Physion: Evaluating physical prediction from vision in humans and machines. *arXiv preprint arXiv:2106.08261*, 2021.
- [6] Florian Bordes, Quentin Garrido, Justine T Kao, Adina Williams, Michael Rabbat, and Emmanuel Dupoux. Intphys 2: Benchmarking intuitive physics understanding in complex synthetic environments. *arXiv preprint arXiv:2506.09849*, 2025.
- [7] Susan Carey. *The origin of concepts*. Oxford University Press, 2011.
- [8] Sili Chen, Hengkai Guo, Shengnan Zhu, Feihu Zhang, Zilong Huang, Jiashi Feng, and Bingyi Kang. Video depth anything: Consistent depth estimation for super-long videos. *2025 IEEE/CVF Conference on Computer Vision and Pattern Recognition (CVPR)*, pages 22831–22840, 2025.
- [9] Zhenfang Chen, Shilong Dong, Kexin Yi, Yunzhu Li, Mingyu Ding, Antonio Torralba, Joshua B. Tenenbaum, and Chuang Gan. Compositional physical reasoning of objects and events from videos. *arXiv preprint arXiv:2408.02687*, 2025.
- [10] Zhenfang Chen, Jiayuan Mao, Jiajun Wu, Kwan-Yee Kenneth Wong, Joshua B Tenenbaum, and Chuang Gan. Grounding physical concepts of objects and events through dynamic visual reasoning. 2021.
- [11] Dima Damen, Hazel Doughty, Giovanni Maria Farinella, Sanja Fidler, Antonino Furnari, Evangelos Kazakos, Davide Moltisanti, Jonathan Munro, Toby Perrett, Will Price, and Michael Wray. Scaling egocentric vision: The epic-kitchens dataset. In *European Conference on Computer Vision (ECCV)*, 2018.
- [12] David Ding, Felix Hill, Adam Santoro, and Matt Botvinick. Object-based attention for spatio-temporal reasoning: Outperforming neuro-symbolic models with flexible distributed architectures. *arXiv preprint arXiv:2012.08508*, 2020.
- [13] Chenyou Fan, Xiaofan Zhang, Shu Zhang, Wensheng Wang, Chi Zhang, and Heng Huang. Heterogeneous memory enhanced multimodal attention model for video question answering. 2019.
- [14] Daniel J Felleman and David C Van Essen. Distributed hierarchical processing in the primate cerebral cortex. *Cerebral cortex*, 1(1):1–47, 1991.
- [15] Rohit Girdhar and Deva Ramanan. Cater: A diagnostic dataset for compositional actions and temporal reasoning. In *International Conference on Learning Representations (ICLR)*, 2020.

[16] Melvyn A Goodale and A David Milner. Separate visual pathways for perception and action. *Trends in Neurosciences*, 15(1):20–25, 1992.

[17] Donald O. Hebb. *The Organization of Behavior: A Neuropsychological Theory*. John Wiley & Sons, New York, 1949.

[18] Gregory Hickok and David Poeppel. The cortical organization of speech processing. *Nature Reviews Neuroscience*, 8(5):393–402, 2007.

[19] Drew A Hudson and Christopher D Manning. Compositional attention networks for machine reasoning. 2018.

[20] Jingwei Ji, Ranjay Krishna, Li Fei-Fei, and Juan Carlos Niebles. Action genome: Actions as compositions of spatio-temporal scene graphs. In *Proceedings of the IEEE/CVF Conference on Computer Vision and Pattern Recognition (CVPR)*, pages 10241–10250, 2020.

[21] Justin Johnson, Bharath Hariharan, Laurens Van Der Maaten, Judy Hoffman, Li Fei-Fei, C Lawrence Zitnick, and Ross Girshick. Inferring and executing programs for visual reasoning. pages 2989–2998, 2017.

[22] Ian T Jolliffe and Jorge Cadima. *Principal component analysis*. Springer, 2016.

[23] Laura Kotovsky and Renee Baillargeon. The development of calibration-based reasoning about collision events in young infants. *Cognition*, 67(3):311–351, 1998.

[24] Dwight J Kravitz, Kadharbatcha S Saleem, Chris I Baker, and Mortimer Mishkin. A new neural framework for visuospatial processing. *Nature Reviews Neuroscience*, 12(4):217–230, 2011.

[25] Brenden M. Lake, Tomer D. Ullman, Joshua B. Tenenbaum, and Samuel J. Gershman. Building machines that learn and think like people. *arXiv preprint arXiv:1604.00289*, 2016.

[26] Thao Minh Le, Vuong Le, Svetha Venkatesh, and Truyen Tran. Hierarchical conditional relation networks for video question answering. pages 9972–9981, 2020.

[27] Jie Lei, Licheng Yu, Mohit Bansal, and Tamara L Berg. Tqvqa: Localized, compositional video question answering. 2018.

[28] Amir Lerer, Shai Gross, and Rob Fergus. Learning physical intuition of block towers by example. In *Proceedings of the 33rd International Conference on Machine Learning*, pages 430–438. JMLR.org, 2016.

[29] Alan M Leslie and Stephanie Keeble. Do six-month-old infants perceive causality? *Cognition*, 25(3):265–288, 1987.

[30] Yijiang Li, Qingying Gao, Tianwei Zhao, Bingyang Wang, Haoran Sun, Haiyun Lyu, Dezhi Luo, and Hokin Deng. Core knowledge deficits in multi-modal language models. *arXiv preprint arXiv:2410.10855*, 2025.

[31] David Mascharka, Philip Tran, Ryan Soklaski, and Arjun Majumdar. Transparency by design: Closing the gap between performance and interpretability in visual reasoning. pages 4942–4950, 2018.

[32] Junbo Niu, Yifei Li, Ziyang Miao, Chunjiang Ge, Yuanhang Zhou, Qihao He, Xiaoyi Dong, Haodong Duan, Shuangrui Ding, Rui Qian, Pan Zhang, Yuhang Zang, Yuhang Cao, Conghui He, and Jiaqi Wang. Ovo-bench: How far is your video-llms from real-world online video understanding? In *2025 IEEE/CVF Conference on Computer Vision and Pattern Recognition (CVPR)*, pages 18902–18913, 2025.

[33] Alec Radford, Jong Wook Kim, Chris Hallacy, Aditya Ramesh, Gabriel Goh, Sandhini Agarwal, Girish Sastry, Amanda Askell, Pamela Mishkin, Jack Clark, et al. Learning transferable visual models from natural language supervision. *arXiv preprint arXiv:2103.00020*, 2021.

[34] R. Riochet, M. Y. Castro, M. Bernard, A. Lerer, R. Fergus, V. Izard, and E. Dupoux. Intphys: A framework and benchmark for visual intuitive physics reasoning. *arXiv preprint arXiv:1803.07616*, 2018.

[35] Giacomo Rizzolatti and Laila Craighero. The mirror-neuron system. *Annual Review of Neuroscience*, 27:169–192, 2004.

[36] Alan Slater, Alan Mattock, and Elizabeth Brown. Size constancy at birth: Newborn infants’ responses to retinal and real size. *Journal of Experimental Child Psychology*, 49(2):314–322, 1990.

[37] Elizabeth S Spelke. Origins of knowledge. *Psychological review*, 99(4):605–632, 1992.

[38] Elizabeth S Spelke. Initial knowledge: Six suggestions. *Cognition*, 50(1-3):431–445, 1994.

[39] Elizabeth S Spelke and Katherine D. Kinzler. Core knowledge. *Developmental Science*, 10(1):89–96, 2007.

[40] Anne M. Treisman and Garry Gelade. A feature-integration theory of attention. *Cognitive Psychology*, 12(1):97–136, 1980.

[41] H.-Y. Tung, M. Ding, Z. Chen, D. Bear, C. Gan, J. B. Tenenbaum, D. L. Yamins, J. E. Fan, and K. A. Smith. Physion++: Evaluating physical scene understanding that requires online inference of different physical properties. *arXiv preprint arXiv:2306.15668*, 2023.

[42] Eloisa Valenza, Irene Leo, Lucia Gava, and Francesca Simon. Perceptual completion in newborn human infants. *Child Development*, 77(6):1810–1821, 2006.

[43] Alexander Veicht, Paul-Edouard Sarlin, Philipp Lindenberger, and Marc Pollefeys. GeoCalib: Single-image Calibration with Geometric Optimization. In *ECCV*, 2024.

[44] Yi Wang, Xinhao Li, Ziang Yan, Yinan He, Jiahuo Yu, Xiangyu Zeng, Chenting Wang, Changlian Ma, Haian Huang, Jianfei Gao, Min Dou, Kai Chen, Wenhui Wang, Yu Qiao, Yali Wang, and Limin Wang. Internvideo2.5: Empowering video mllms with long and rich context modeling. *arXiv preprint arXiv:2501.12386*, 2025.

[45] Zhiyu Wu, Xiaokang Chen, Zizheng Pan, Xingchao Liu, Wen Liu, Damai Dai, Huazuo Gao, Yiyang Ma, Chengyue Wu, Bingxuan Wang, Zhenda Xie, Yu Wu, Kai Hu, Jiawei Wang, Yaofeng Sun, Yukun Li, Yishi Piao, Kang Guan, Aixin Liu, Xin Xie, Yuxiang You, Kai Dong, Xingkai Yu, Haowei Zhang, Liang Zhao, Yisong Wang, and Chong Ruan. Deepseek-vl2: Mixture-of-experts vision-language models for advanced multimodal understanding. *arXiv preprint arXiv:2412.10302*, 2024.

[46] An Yang, Anfeng Li, Baosong Yang, Beichen Zhang, Binyuan Hui, Bo Zheng, Bowen Yu, Chang Gao, Chegen Huang, Chenxu Lv, Chujie Zheng, Dayiheng Liu, Fan Zhou, Fei Huang, Feng Hu, Hao Ge, Haoran Wei, Huan Lin, Jialong Tang, Jian Yang, Jianhong Tu, Jianwei Zhang, Jianxin Yang, Jiaxi Yang, Jing Zhou, Jingren Zhou, Junyang Lin, Kai Dang, Keqin Bao, Kexin Yang, Le Yu, Lianghao Deng, Mei Li, Mingfeng Xue, Mingze Li, Pei Zhang, Peng Wang, Qin Zhu, Rui Men, Ruize Gao, Shixuan Liu, Shuang Luo, Tianhao Li, Tianyi Tang, Wenbiao Yin, Xingzhang Ren, Xinyu Wang, Xinyu Zhang, Xuancheng Ren, Yang Fan, Yang Su, Yichang Zhang, Yinger Zhang, Yu Wan, Yuqiong Liu, Zekun Wang, Zeyu Cui, Zhenru Zhang, Zhipeng Zhou, and Zihan Qiu. Qwen3 technical report. *arXiv preprint arXiv:2505.09388*, 2025.

[47] Fei Yang. Automatic extraction of relationships among motivations, emotions and actions from natural language texts. In *Proceedings of the 38th Pacific Asia Conference on Language, Information and Computation*, pages 1117–1128, Tokyo, Japan, December 2024. Tokyo University of Foreign Studies.

[48] Fei Yang. Propnet: a white-box and human-like network for sentence representation. *arXiv preprint arXiv:2502.10725*, 2025.

[49] Kexin Yi, Chuang Gan, Yunzhu Li, Pushmeet Kohli, Jiajun Wu, Antonio Torralba, and Joshua B. Tenenbaum. CLEVRER: collision events for video representation and reasoning. In *ICLR*, 2020.

[50] Kexin Yi, Chuang Gan, Yunzhu Li, Pushmeet Kohli, Jiajun Wu, Antonio Torralba, and Joshua B Tenenbaum. Clevrer: Collision events for video representation and reasoning. 2020.

[51] Xiangyu Zeng, Kunchang Li, Chenting Wang, Xinhao Li, Tianxiang Jiang, Ziang Yan, Songze Li, Yansong Shi, Zhengrong Yue, Yi Wang, Yali Wang, Yu Qiao, and Limin Wang. Timesuite: Improving mllms for long video understanding via grounded tuning. In *International Conference on Representation Learning*, volume 2025, pages 38057–38081, 2025.

[52] Boqiang Zhang, Kehan Li, Zesen Cheng, Zhiqiang Hu, Yuqian Yuan, Guanzheng Chen, Sicong Leng, Yuming Jiang, Hang Zhang, Xin Li, Peng Jin, Wenqi Zhang, Fan Wang, Lidong Bing, and Deli Zhao. Videollama 3: Frontier multimodal foundation models for image and video understanding. *arXiv preprint arXiv:2501.13106*, 2025.

A YOLO Models

We annotated shape and texture bounding boxes for 190 randomly selected frames from CLEVRER training videos using LabelImg, a Python package for image annotation. The frame set is distributed as follows: 25% contain boundary objects, 25% contain obstructed objects, and the remaining 50% contain only normal objects (without boundary or obstruction). The data was split into 160 training and 30 validation images. Two separate YOLO11m models were trained for shape and texture detection with the following parameters: shape model ($lr=0.002$, epochs=20, batch=4) and texture model ($lr=0.005$, epochs=20, batch=4). Both models achieved near-perfect detection performance across all categories, which is presented in Tab. 4.

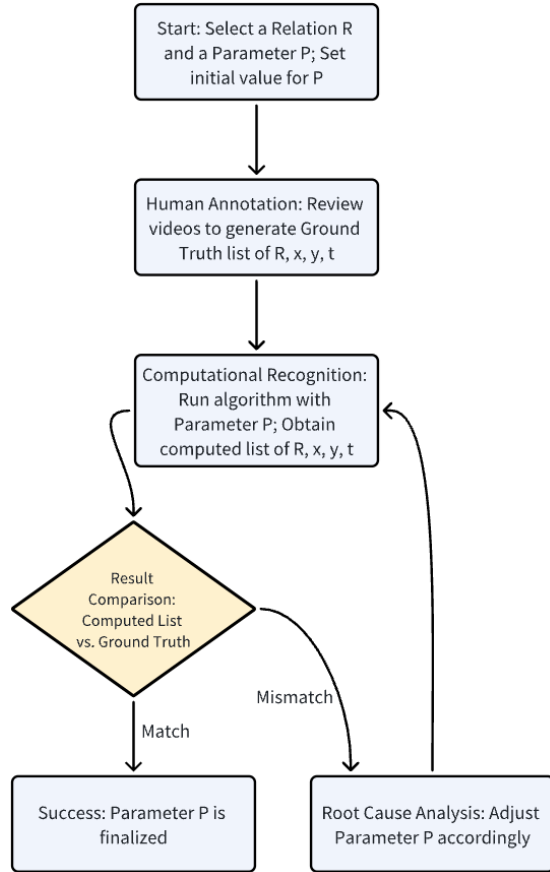


Figure 5: Human-Driven Parameter Tuning Loop. In the list notation, entities x and y participate in relation R at time slot t .

B Model Parameters

The threshold parameters for each relation are determined in a human-driven fashion, guided by human perceptual judgments to ensure consistency. We

Table 4: Detection performance of shape and texture models

Model	Class	Precision	Recall
Shape	Sphere	1.000	0.996
	Cube	0.994	1.000
	Cylinder	0.986	1.000
Texture	Rubber	0.999	1.000
	Metal	0.999	1.000

Table 5: Direction Labels and Corresponding Angle Intervals

Direction	Angle Interval (degrees)
Front	(-22.5, 22.5]
Front-right	(22.5, 67.5]
Right	(67.5, 112.5]
Back-right	(112.5, 157.5]
Back (positive)	(157.5, 180]
Back (negative)	(-180, -157.5]
Back-left	(-157.5, -112.5]
Left	(-112.5, -67.5]
Front-left	(-67.5, -22.5]

calibrate these parameters using 10 videos from the CLEVRER training set and validate the computing result of the relation against human observations, with the detailed process shown in Fig. 5. Tab. 6 presents core parameter definitions and their values after tuning.

C Direction Labels

Tab. 5 shows the angle interval for each direction label. The back direction is split into two separate intervals—Back (positive) and Back (negative)—due to the circular nature of angular measurements. In a standard angular coordinate system, angles wrap around at $\pm 180^\circ$, meaning that -180° and $+180^\circ$ represent the same physical direction (directly behind). This discontinuity necessitates dividing the back region into two intervals to maintain mathematical consistency while covering the complete 45° angular span centered at 180° (or equivalently, -180°). The positive interval $(157.5, 180]$ covers angles approaching from the right side, while the negative interval $(-180, -157.5]$ covers angles approaching from the left side, together forming a continuous back-facing sector.

Table 6: SRNN Parameter Configurations

Parameter Setting	Description
ATTENTION_IOU_THD = 0.85	Bounding-box overlap threshold for attribute binding (IoU)
COLOR_FOCUS_AREA_RATIO = 0.7	Ratio of the central area used for color recognition
CONFIDENCE_THD = 0.7	Confidence threshold for object detection by YOLO models
FOCAL_LENGTH = 420	Used in transforming pixel coordinates to camera coordinates
BOX_OVERLAP_THD = 0.1	Bounding-box overlap threshold for object tracking (IoU)
MOVE_THD = 0.01	Moving threshold for object kinematic state (Euclidean distance)
DIST_ATT_THD = 0.1	If the minimum distance between two objects exceeds this threshold, the distance change is not attended
MOVING_AVG_WINDOW = 5	Moving average window for computing distance change between two objects
TOUCH_THD = 0.04	Distance threshold for touch detection (Euclidean distance)
TOUCH_BOX_OVERLAP_THD = 0.01	Bounding-box overlap threshold for touch detection (IoU)

D SRNN Examples

Fig. 6 presents an example of our approach for perceiving static properties of objects in a single frame from video_12214. Fig. 7 illustrates the neural network representation corresponding to video_12214. Fig. 8 presents the language generation module for video_12214. Figure 9 presents the textual descriptions for each time slot of video_12214.

E LLM Prompts

We selected Qwen3 [46] as the LLM for CLEVRER question-answering tasks, with the model code qwen3-235b-a22b-instruct-2507. Qwen3 is an open-source large language model that has demonstrated strong performance on reasoning benchmarks.

The prompt comprises Task Definition, Video Description Text, Question Text, Choice Text, Critical Alignments, and Output Format. The prompts of predictive questions, counterfactual questions, descriptive questions, and explanatory questions are shown in Fig. 10, Fig. 11, Fig. 12, and Fig. 13, respectively.

LLM’s understanding of the questions are not

aligned with the question answers. Consider this question “Which of the following is responsible for the gray sphere’s colliding with the purple object”. LLM’s understanding of this question is that only the most recent collision is responsible. However, the ground-truth answer is that all related collisions on the timeline are responsible.

Through iterative error analysis, we identify primary discrepancies between the LLM’s comprehension of questions and the corresponding ground-truth answers, which are subsequently integrated into the prompt.

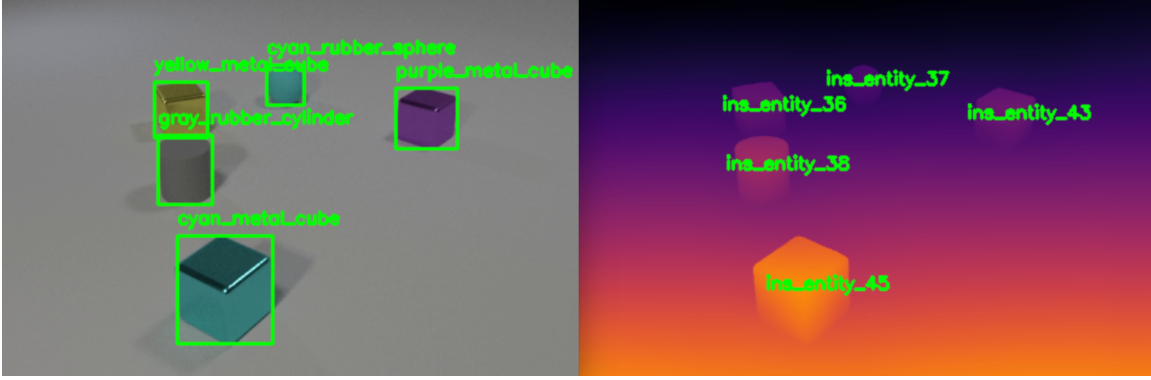


Figure 6: Object detection (left) and depth estimation (right) results in a single CLEVRER video frame. The left panel shows detected object regions—shape and texture—bound into unified representations (e.g., “blue metal sphere”) through IoU-based fusion and color categorization. The right panel presents the corresponding depth map, where each pixel’s depth is estimated using Video Depth Anything.

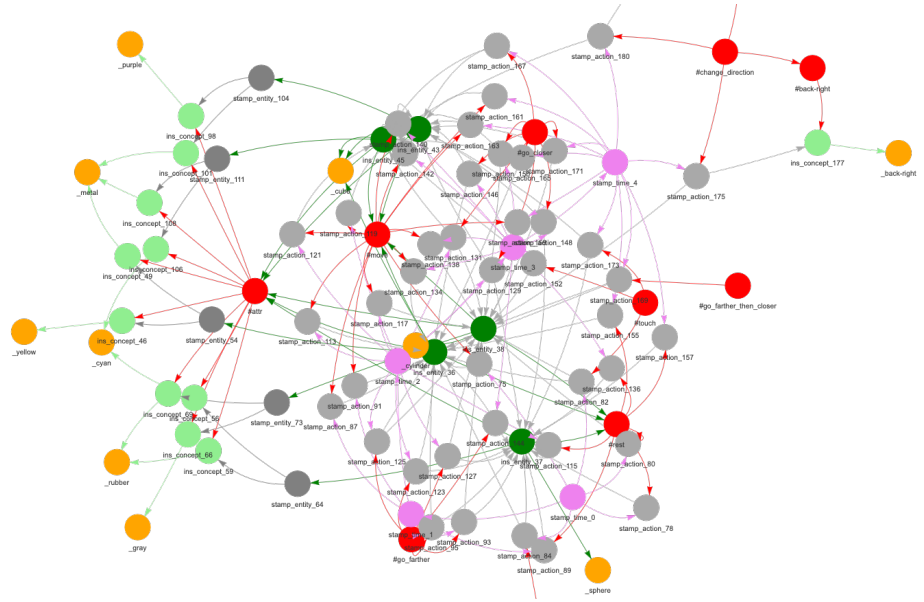


Figure 7: Neural network representation for video_12214. In this representation, neurons are color-coded according to their type: nature neurons are shown in red, stamp neurons in gray, time neurons in purple, instance neurons in green, and lexical neurons in yellow. Deactivated neurons are omitted for clarity. Arrows on the connections indicate the direction of signal transmission upon neuron activation.

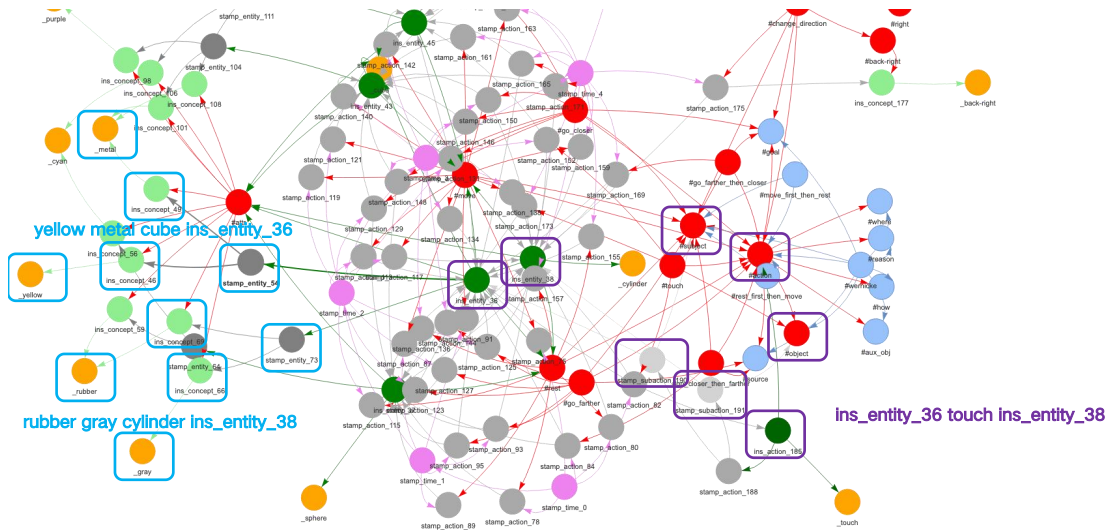


Figure 8: Language generation module for video_12214. **Right:** The purple boxes on the right mark the language generation process for the How Pathway. A neuron named ins_action_185 is created and activated by the neural network, serving as the start point of the semantic network. A connection is established between ins_action_185 and #action by the neural network after the birth of ins_action_185, making ins_action_185 being able to send a signal to #action. The neural network also establishes a connection between ins_action_185 and a lexical neuron _touch. Next, two semantic role neurons #subject and #object are activated by the joint signals from #touch and #action. Finally, stamp_subaction_190 is created to bind ins_entity_36 and #subject. Similarly, stamp_subaction_191 is created to bind ins_entity_38 and #object. The sentence generator outputs a sentence “ins_entity_36 touches ins_entity_38” based on this semantic network. **Left:** The left cyan boxes illustrate the language generation process for the What Pathway. The neuron ins_entity_36 triggers the creation and activation of stamp_entity_54. In the meantime, ins_concept_46, ins_concept_49, etc., are created and activated to record the attributes of this entity, and bound by stamp_entity_54. A phrase “yellow metal cube ins_entity_36” is generated based on this semantic network. Similarly, another phrase “rubber gray cylinder ins_entity_38” is also produced. The sentence generator then merges the outputs from the How Pathway and the What Pathway, ultimately yielding the final sentence: “The yellow metal cube ins_entity_36 touches the rubber gray cylinder ins_entity_38.”

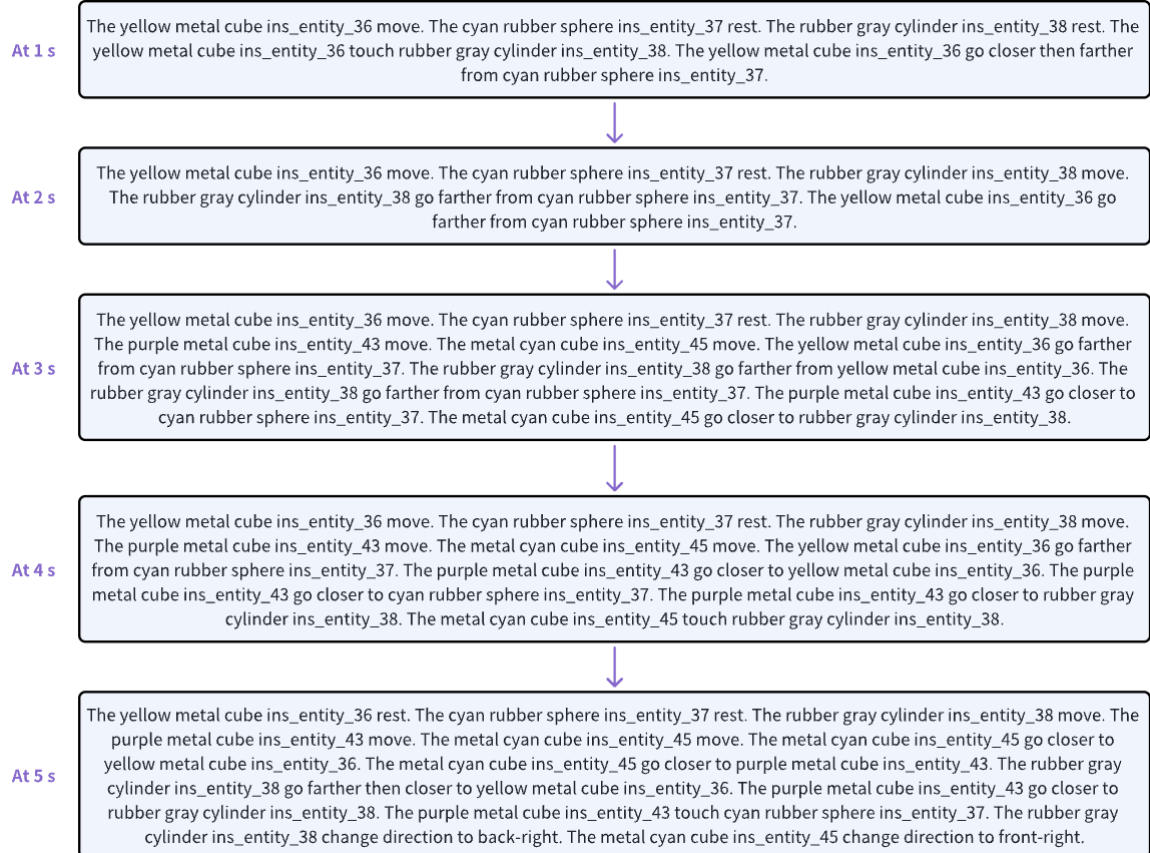


Figure 9: Description text for video_12214. Each segment contains multiple sentences, with each describing a relation depicted in the video.

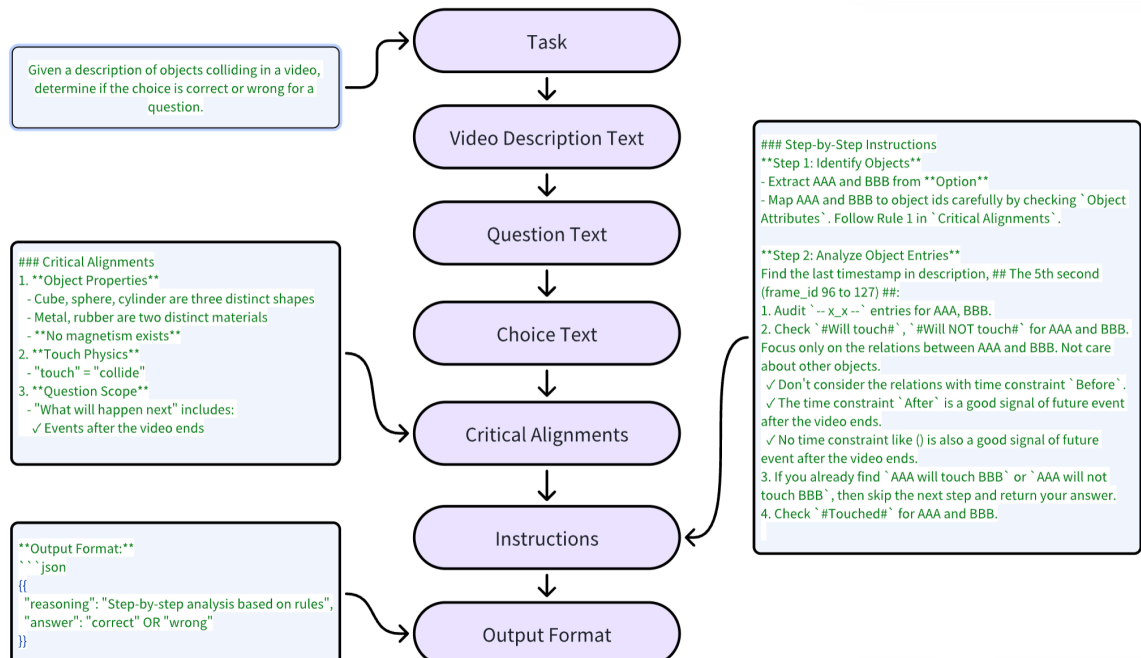


Figure 10: LLM prompt for predictive questions. The corresponding text segments are assembled into a prompt according to the arrow sequence.

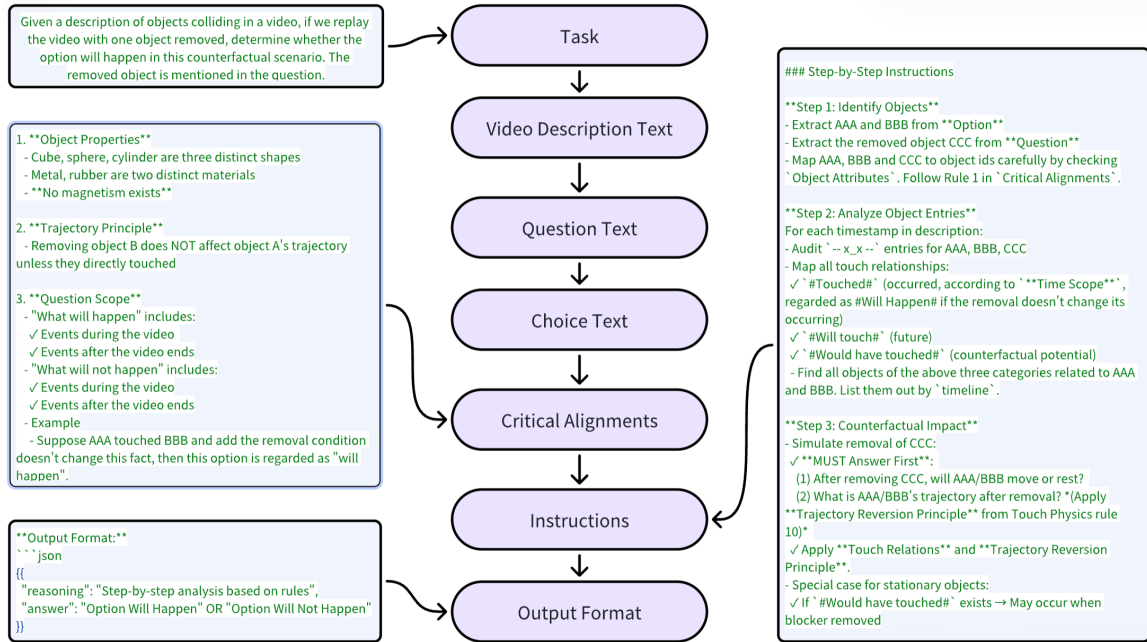


Figure 11: LLM prompt for counterfactual questions. The corresponding text segments are assembled into a prompt according to the arrow sequence.

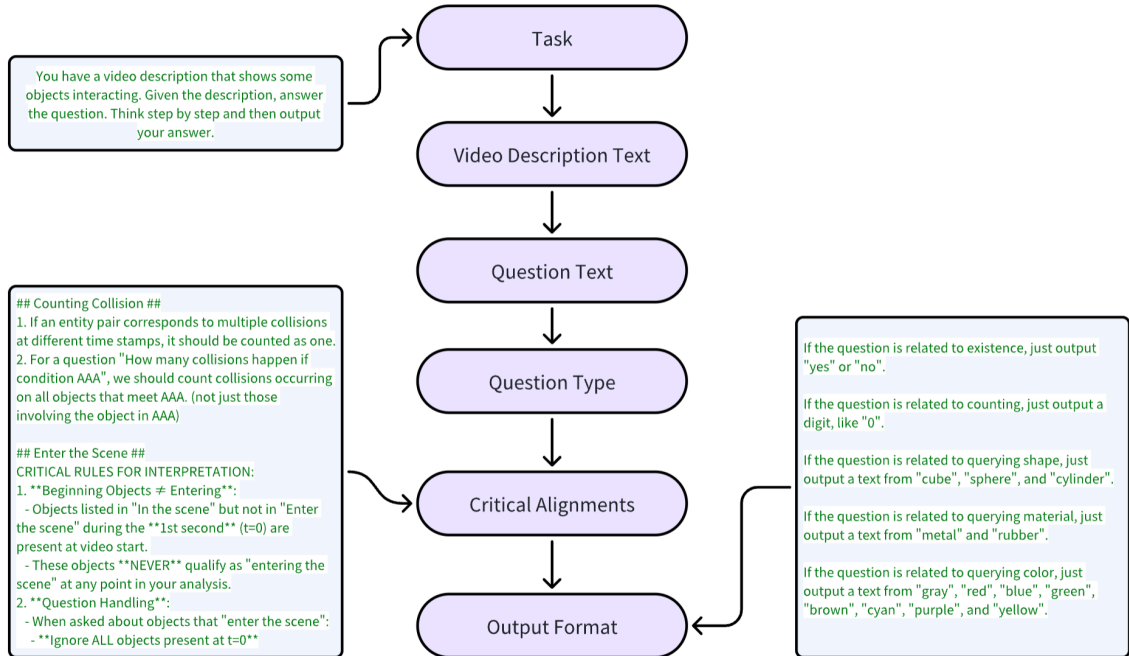


Figure 12: LLM prompt for descriptive questions. The question type of a descriptive question refers to existence, counting, querying shape, querying material or querying color. The corresponding text segments are assembled into a prompt according to the arrow sequence.

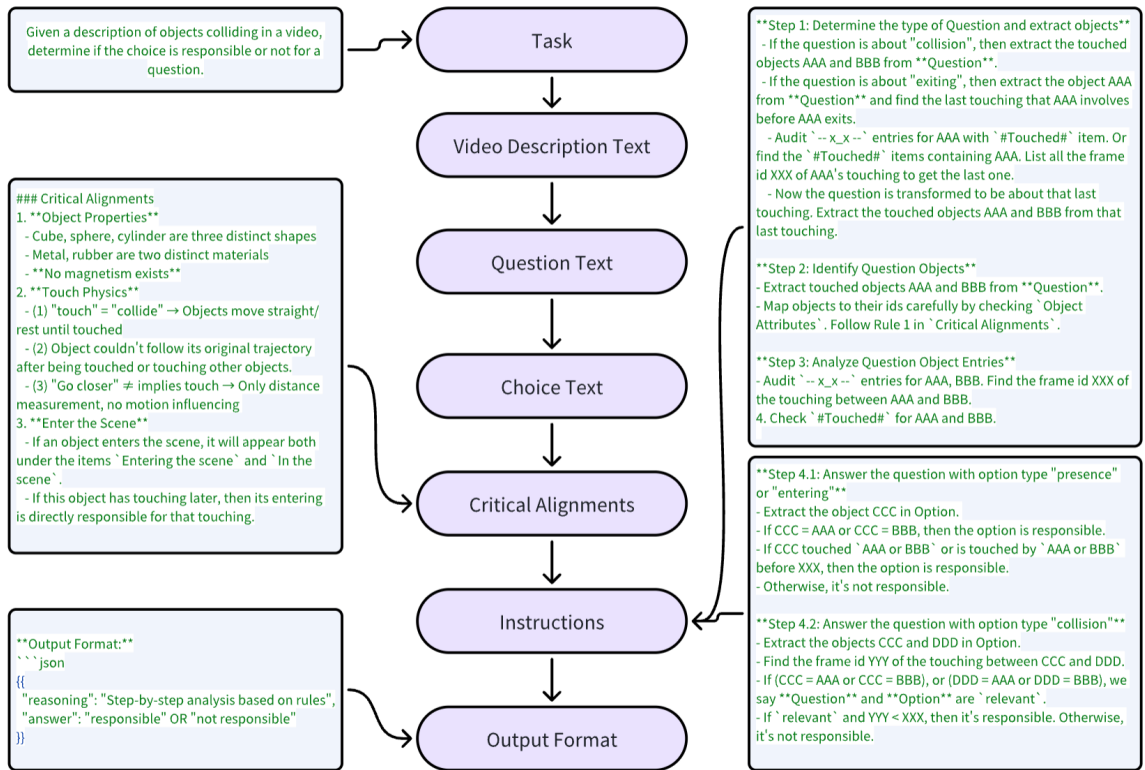


Figure 13: LLM prompt for explanatory questions. The corresponding text segments are assembled into a prompt according to the arrow sequence.